

Connecting the avoided quantum critical point to the magic-angle transition in three-dimensional Weyl semimetals

J. H. Pixley^{1,2}, David A. Huse³, and Justin H. Wilson⁴

¹*Department of Physics and Astronomy, Center for Materials Theory, Rutgers University, Piscataway, New Jersey 08854, USA*

²*Center for Computational Quantum Physics, Flatiron Institute, 162 5th Avenue, New York, New York 10010, USA*

³*Department of Physics, Princeton University, Princeton, New Jersey 08544, USA*

⁴*Department of Physics and Astronomy and Center for Computation and Technology, Louisiana State University, Baton Rouge, Louisiana 70803, USA*



(Received 27 November 2023; accepted 27 March 2024; published 25 April 2024)

We theoretically study the interplay of short-range random and quasiperiodic static potentials on the low-energy properties of three-dimensional Weyl semimetals. This setting allows us to investigate the connection between the semimetal to diffusive metal “magic-angle” phase transition due to quasiperiodicity and the rare-region-induced crossover at an avoided quantum critical point (AQCP) due to disorder. We show that in the presence of both random and quasiperiodic potentials the AQCP becomes lines of crossovers, which terminate at magic-angle critical points in the quasiperiodic, disorder-free limit. We analyze the magic-angle transition by approaching it along these lines of avoided transitions, which unveils a rich miniband structure and several AQCPs. These effects can be witnessed in cold atomic experiments through potential engineering on semimetallic band structures.

DOI: [10.1103/PhysRevB.109.165151](https://doi.org/10.1103/PhysRevB.109.165151)

I. INTRODUCTION

There is a significant push to discover and understand the nature of gapless topological materials. This has been fueled by the experimental discovery of three-dimensional (3D) topological Dirac and Weyl semimetals in weakly correlated narrow-gap semiconductors [1–9], as well as their observation in several strongly correlated materials [10–18]. However, the Fermi energy does not typically coincide with the Weyl or Dirac touching points in the band structure, making the effects on the low-energy thermodynamic properties indirect. Nonetheless, nodal touching points have been identified using a combination of angle-resolved photoelectron spectroscopy experiments [1–3, 19, 20] and *ab initio* calculations [21, 22], while their manifestation in transport arises through a negative magnetoresistance [23–25]. These measurements provide a systematic means to identify the existence of Dirac and Weyl nodes in several weakly correlated material candidates. Recently, the demonstration of a 3D Weyl semimetal in an ultracold atom experiment using artificial spin-orbit coupling [26] opened the door to a new level of control over Weyl semimetals. These systems are tunable; filling is controlled by the number of atoms in the trap, and disorder and lattice imperfections are removed altogether. Therefore, perturbations can be turned on at will to determine the fate of Weyl semimetals experimentally while opening the door to study effects that are out of reach in solid-state compounds.

Due to the interplay of topology and a vanishing pseudogap density of states, single-particle perturbations can have several nontrivial effects. In particular, the effects of disorder on non-interacting Weyl semimetals have been well studied [27, 28]. Within perturbative (e.g., self-consistent Born [29, 30],

large- N [31], and renormalization group [32, 33]) treatments of the problem, a disorder-driven quantum critical point was found. However, when taking into account the nonperturbative effects of disorder, rare regions of the random potential give rise to power-law quasibound states where the disorder is atypically large and cannot be treated perturbatively [34]. These rare states were found to endow the Weyl semimetal with a finite density of states at the Weyl node, destabilizing the Weyl semimetal phase into a diffusive metal for any weak random potential [28]. As a result, it was shown that the putative critical point is rounded out into a crossover, dubbed an avoided quantum critical point (AQCP) [35–38]. Instanton fluctuation calculations (about the saddle point) for a single Weyl cone found that this picture is modified [39], and these results were interpreted in terms of a nontrivial scattering phase shift [40]. However, it was later shown that such phase shifts are inherently problematic as their conclusions violate Levinson’s theorem [41] and, instead, the AQCP is the correct description [42]. This is also consistent with a numerical study of a disordered single Weyl cone in the continuum limit that showed the transition remains strongly avoided with essentially the same kind of AQCP as in previously studied lattice models with multiple Weyl cones [43].

On the other hand, the fate of Weyl semimetals in the presence of quasiperiodicity that does not have any rare regions (due to the potential being infinitely long range correlated) was only considered recently. It was numerically shown [44] and then rigorously proven [45] that the Weyl semimetal phase is stable to a weak quasiperiodic potential. As a result, at a large enough potential strength quasiperiodicity drives a bona fide semimetal to diffusive metal phase transition at a nonzero critical quasiperiodic strength [44]. At this

transition the Weyl velocity goes to zero continuously, the density of states becomes nonanalytic, and the single-particle wave functions at the Dirac node energy delocalize in momentum space. Studies of similar effects in two-dimensional Dirac semimetal models [46–48] have linked this quantum phase transition to the magic-angle phenomena originally discovered in twisted bilayer graphene [49] (and extended to incorporate incommensurate effects [46,50]). Thus, the transition that was originally sought in disordered Weyl semimetals was uncovered in the quasiperiodic limit by removing rare regions from the problem. We therefore refer to the critical point due to a quasiperiodic potential as a “magic-angle transition” (MAT); here the “angle” refers to the incommensurate wave vector characterizing the quasiperiodic potential that can be viewed as an angle within a higher-dimensional projective quasicrystal construction [51].

In this paper, we make a direct link between the avoided transition and the magic-angle quantum critical point in three dimensions. We do so by considering how the avoided transition is connected to the magic-angle condition of a vanishing velocity by studying the interplay of disorder and quasiperiodicity on equal footing. A closely related problem has been studied in two-dimensional Dirac semimetal models and is pertinent to understand the role of twist disorder in magic-angle graphene experiments [50,52–56], which have attracted a great deal of attention. However, in two dimensions the marginal relevance of disorder removes the AQCP from the problem and does not allow a direct link between the two effects to be exposed.

Through numerical calculations of the density of states of an inversion-broken 3D Weyl semimetal using the kernel polynomial method (KPM) we show that the AQCP becomes a line of crossovers that terminate at the MAT, as shown in the phase diagram in Fig. 1. We study the fate of the analytic properties of the zero-energy density of states when disorder is added to the quasiperiodic Weyl semimetal model, demonstrating the interplay of incommensurate induced miniband formation and nonperturbative rare-region effects. Last, the critical properties of the magic-angle transition are determined by approaching it along the crossover line of avoided transitions, which allows us to provide an accurate estimate of the power law nature of the vanishing Weyl velocity.

The remainder of this paper is organized as follows: The model and the method used are introduced in Sec. II, and we determine the phase diagram of the model in Sec. III and the critical properties along the line of crossovers in Sec. IV. Finally, in Sec. V we discuss the implications of our results and how to detect our predictions using ultracold atoms and conclude. In the Appendix we briefly discuss the formation of the first and second minibands in the absence of disorder.

II. MODEL AND METHOD

To investigate the interplay of the effects of disorder and quasiperiodicity on Weyl semimetals we add two separate potentials to a lattice model of an inversion-symmetry-broken Weyl semimetal given by

$$H = \sum_{\mathbf{r}, \mu} (it_{\mu} \psi_{\mathbf{r}}^{\dagger} \sigma_{\mu} \psi_{\mathbf{r}+\hat{\mu}} + \text{H.c.}) + \sum_{\mathbf{r}} \psi_{\mathbf{r}}^{\dagger} V(\mathbf{r}) \psi_{\mathbf{r}}, \quad (1)$$

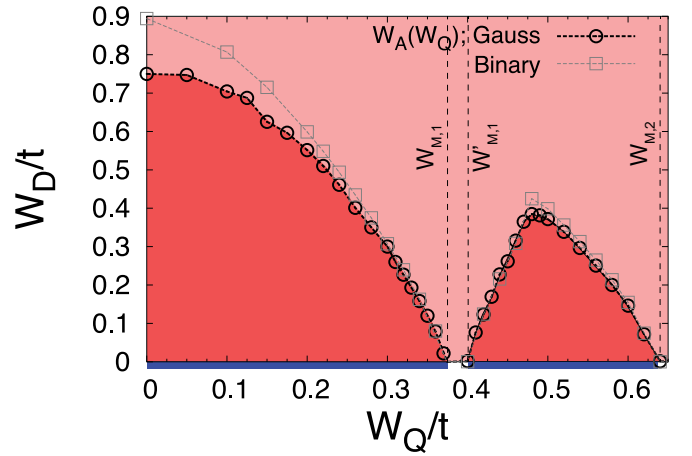


FIG. 1. Phase diagram of disorder (W_D) and quasiperiodic (W_Q) potential strengths at the Weyl node energy ($E = 0$). Solid blue lines are stable Weyl semimetal phases that terminate at magic-angle transitions (the Weyl semimetal at larger W_Q is an inverted semimetal phase). At any nonzero W_D the model is in the diffusive metal phase; dark red marks the semimetal regime $\rho(E) \approx \rho(0) + \rho''(0)E^2/2$, where $\rho(0)$ is nonzero but exponentially small, and light red is past the AQCP where $\rho(0) \sim O(1)$. The location of the peak in $\rho''(0)$ as a function of W_D (for fixed W_Q) provides an estimate of the AQCP (and the quasiperiodic transition at $W_D = 0$) that we label as $W_A(W_Q)$. We compare two choices of the distribution of the disorder potential $P[V]$, showing their distinction is insignificant near the magic-angle transitions and Gaussian and binary distributions; the latter has been shown to weaken the avoidance for $W_Q = 0$ [36]. This analysis is done on a system size of $L = 89$, KPM expansion order $N_C = 2^{10}$, and 100 samples. Sufficiently close to the magic-angle transitions additional minibands appear that give rise to more structure in $W_A(W_Q)$ (see Sec. IV); that additional miniband structure is not shown here. Dashed vertical lines indicate the transitions at $W_D = 0$ into or out of diffusive phases (from left to right, $W_{M,1} \approx 0.38t$, $W'_{M,1} \approx 0.395t$, and $W_{M,2} \approx 0.6345t$).

where $\mu = x, y, z$ and the potential is a sum of two separate contributions from randomness (that we denote with D for disorder) and quasiperiodicity Q ,

$$V(\mathbf{r}) = V_D(\mathbf{r}) + V_Q(\mathbf{r}), \quad (2)$$

which we parametrize below. The model lives on the simple cubic lattice of linear size L , and we average over twisted boundary conditions to reduce finite-size effects. The hopping is then given by $t_{\mu} = t e^{i\theta_{\mu}/L}/2$, where the twist in the μ direction θ_{μ} is randomly sampled between 0 and 2π . In the absence of the potentials the band structure is given by

$$E_0(\mathbf{k}) = \pm t \sqrt{\sum_{\mu=x,y,z} \sin^2(k_{\mu} + \theta_{\mu}/L)}, \quad (3)$$

with eight Weyl cones labeled by \mathbf{K}_W at the time-reversal-invariant momenta (for no twist) in the Brillouin zone. Near each Weyl point \mathbf{K}_W the dispersion is given by

$$E_0(\mathbf{k}) \approx \pm v_0(\mathbf{K}_W) |\mathbf{k} - \mathbf{K}_W|, \quad (4)$$

with a velocity $v_0(\mathbf{K}_W) = \pm t$ that depends on the helicity.

The disorder potential $V_D(\mathbf{r})$ is sampled independently at each site from a probability distribution $P[V]$. In the following

we consider two different distributions. To enhance rare-region effects we consider a Gaussian distribution with zero mean and standard deviation W_D . To suppress rare regions and enhance the critical scaling properties we also consider a binary distribution where the value of the potential is equally likely to be $\pm W_D$. In the absence of the quasiperiodic potential the semimetal phase of this model is unstable to rare-region effects that induce a diffusive metal phase at infinitesimal disorder strength. The resulting perturbative transition is avoided and rounded into a crossover. By varying the tails of the distribution $P[V]$ we can control the probability to generate rare events, removing the tails as in the binary case quantitatively suppresses (but does not eliminate) rare-region effects [36]. All results shown are for the case of Gaussian disorder unless otherwise specified.

The quasiperiodic potential is given by

$$V_Q(\mathbf{r}) = W_Q \sum_{\mu=x,y,z} \cos(Q_L r_\mu + \phi_\mu), \quad (5)$$

where the quasiperiodic wave vector is taken as a rational approximant $Q_L = 2\pi F_{n-2}/L$, where the system size is given by the n th Fibonacci number $L = F_n$ and in the thermodynamic limit $Q_L \rightarrow Q = 2\pi[2/(\sqrt{5} + 1)]^2$. The random phases ϕ_μ are randomly sampled between 0 and 2π as the origin of the quasiperiodic potential is arbitrary. In the absence of the random potential this model has been shown to host several magic-angle transitions between Weyl semimetal and diffusive metal phases as a function of increasing W_Q . Near the magic-angle transition W_c , in the semimetallic phase, the velocity of the Weyl cone vanishes as

$$v(W_Q) \sim |W_Q - W_c|^{\beta/d}, \quad (6)$$

where $\beta \approx 2$ and $d = 3$ is the spatial dimension [44]. The plane wave Weyl eigenstates delocalize in momentum space, and the level statistics become consistent with random matrix theory when one enters the diffusive metallic phase. In the following, we use disorder to round out the critical properties of the quasiperiodic induced transition, which allows us to approach the MAT from a new direction.

To characterize the system we numerically compute the density of states (DOS), which is given by

$$\rho(E) = \frac{1}{L^3} \sum_i \delta(E - E_i), \quad (7)$$

where E_i are the eigenenergies of H . The DOS is computed using the KPM by expanding it in terms of Chebyshev polynomials to order N_C and evaluating the expansion coefficients with sparse matrix-vector multiplication. For the system sizes $L = 55, 89$ considered here, N_C is the most dominant finite-size effect, and therefore, we try to converge our results with N_C . The analytic properties of the density of states are investigated by assuming the DOS is always analytic and Taylor expanding

$$\rho(E) = \rho(0) + \frac{1}{2}\rho''(0)E^2 + \dots, \quad (8)$$

and we directly compute the second derivative of the DOS with the KPM at the Weyl node energy ($E = 0$) $\rho''(0)$ [36]. If the DOS becomes nonanalytic, then $\rho''(0) \rightarrow \infty$, whereas if the system undergoes a crossover, it will remain finite.

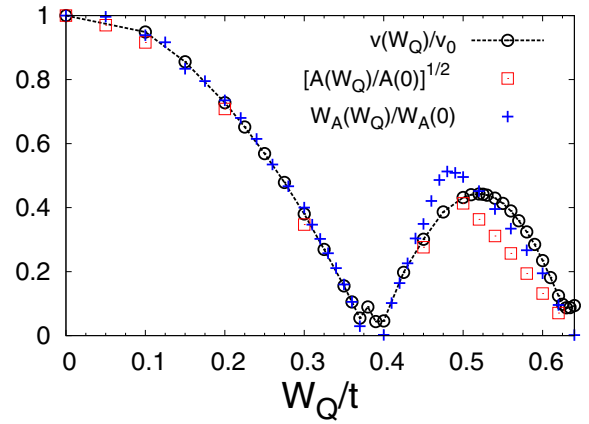


FIG. 2. Renormalized velocity and related scales: Comparison of the renormalized velocity $v(W_Q)$ with the location of the avoided transition $W_A(W_Q)$ and the dependence of the density of states $A(W_Q)$ [see Eq. (12)]. The velocity $v(W_Q)$ of the renormalized semimetal is obtained from the disorder-free limit using $\rho''(0) \propto v^{-3}$ (for system size $L = 144$ and $N_C = 2^{10}$ from Ref. [44]), $A(W_Q)$ is extracted from the rare-region dependence of $\ln \rho(0) \sim A(W_Q)/(W_D)^2$ [from the data that are converged in L and N_C ; see Eq. (12)], and $W_A(W_Q)$ denotes the line of AQCPs determined from the maximum in $\rho''(0)$ as a function of W_D (obtained from a system size of $L = 89$ and KPM expansion order $N_C = 2^{10}$). Sufficiently close to each MAT, the formation of minibands (see the Appendix) enriches the picture beyond the relations implied by these data; that requires sufficiently large L and/or N_C to observe (see Sec. IV).

For a stable Weyl semimetal phase we have $\rho(0) = 0$ and $\rho''(0) = N_W/(2\pi^2 v^3)$, where v is the velocity of the Weyl cone and N_W denotes the number of Weyl points in the band structure. Using this relation, an estimate of the velocity in the Weyl semimetal phase $W_D = 0$ is shown in Fig. 2. Importantly, this also implies that when $v \rightarrow 0$, the DOS becomes nonanalytic as $\rho''(0) \rightarrow \infty$, signaling a MAT. Thus, Fig. 2 also demonstrates the existence of three MATs taking place at $W_{M,1} \approx 0.38t$ into the diffusive metal (DM) phase and out of the DM phase to a reentrant semimetal (SM) at $W'_{M,1} \approx 0.395t$ and then a transition back to the DM phase at $W_{M,2} \approx 0.6345t$ for this range of W_Q and $Q/2\pi = [2/(\sqrt{5} + 1)]^2$. We note that the reentrant semimetal phase for $W > W'_{M,1}$ occurs by inverting the positive and negative energy bands, which we refer to as an inverted Weyl semimetal phase. In Ref. [44] we demonstrated that the critical properties of each of these quasiperiodic driven transitions is the same (to within numerical accuracy). The structure of the phase diagram (e.g., the number of magic-angle transitions) depends on the choice of Q_L in Eq. (5) [44,46]. Predicting the structure of the phase diagram to this level requires higher-order perturbative corrections [the leading order given in the following section, Eq. (9), contains only one].

III. PHASE DIAGRAM

As the Weyl semimetal phase is stable in the presence of a quasiperiodic potential, we find it most natural to explain the structure of the phase diagram at the Weyl node energy by adding disorder to the quasiperiodic Weyl semimetal model.

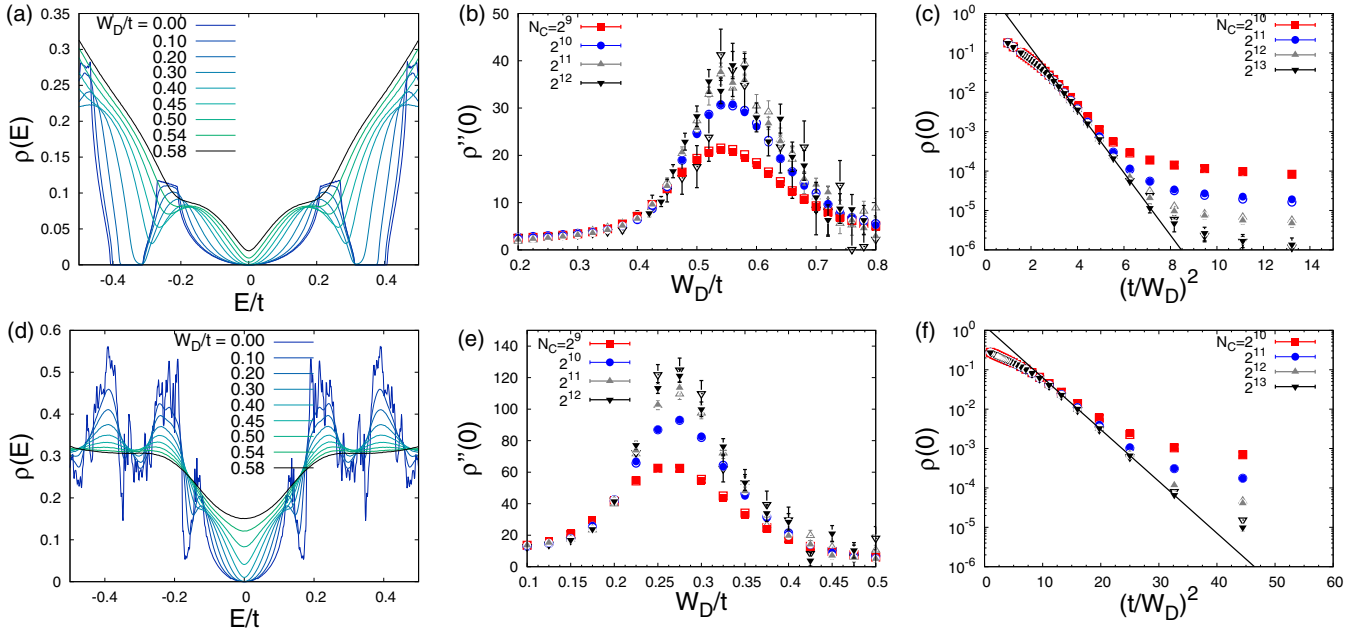


FIG. 3. Evolution of the density of states: (a) and (d) $\rho(E)$ (with $L = 89$ and $N_C = 2^{13}$), (b) and (e) $\rho''(0)$, and (c) and (f) $\rho(0)$ as a function of W_D and W_Q for various values of the KPM expansion order N_C , $L = 55$ (open symbols), and $L = 89$ (solid symbols). The values of the quasiperiodic potential are $W_Q = 0.2t$ in the semimetal phase (top row) and $W_Q = 0.55t$ in the inverted semimetal phase (bottom row). These data are averaged over 1000 samples for $N_C = 2^9, 2^{10}, 2^{11}$ and 5000 samples for $N_C = 2^{12}, 2^{13}$. Straight lines in (c) and (f) are fits to the rare-region form in Eq. (12).

From this perspective, we can safely use perturbation theory to determine a new low-energy effective model in the quasiperiodic renormalized semimetal phase. We note that for $W'_{M,1} < W_Q < W_{M,2}$ the inverted semimetal phase requires a rather high order in perturbation theory to be described. For $W_D = 0$ we can evaluate the self-energy of the single-particle Green's function by treating W_Q perturbatively [46], similar to what is done to describe twisted bilayer graphene [49]. Focusing on the present case with Q close to π , we need to consider only internode scattering. This results in a renormalized velocity $v(W_Q)$, with a perturbative expression to leading order [46]

$$\frac{v(W_Q)}{v_0} \approx \frac{1 - 2(2 - \cos(Q))\alpha^2}{1 + 6\alpha^2}, \quad (9)$$

where the dimensionless coupling constant $\alpha = W/[2t \sin(Q)]$ and a magic-angle condition occurs where $v(W_Q = W_{MA}) = 0$. We note that sufficiently high orders in perturbation theory are required to describe the data in Fig. 2. Nonetheless, our numerical results confirm beyond perturbation theory that the quasiperiodic potential produces a magic-angle transition where the velocity vanishes. At the same time, away from the magic-angle transition the quasiperiodic potential carves out a mini Brillouin zone (mBZ), with an effective band structure on an emergent moiré lattice that is qualitatively described by perturbation theory (see Refs. [46,57] for an explicit construction of the band structure along these lines as well as the Appendix for more details).

The band gap in the density of states in Fig. 3(a) for $W_D = 0$ and $W_Q = 0.2t$ demonstrates the stability of the Weyl semimetal phase to a weak quasiperiodic potential at low energies and the presence of the mBZ. As we will demonstrate

below, our numerical results in a portion of the weakly disordered semimetal phases of the model can thus be interpreted as introducing disorder to a Weyl semimetal that lives on the mBZ with a renormalized velocity $v(W_Q)$. At larger quasiperiodic strength, in particular, in the reentrant semimetallic phase with $W_Q \gtrsim 0.5t$, this is modified due to the inversion of the bands and the lack of a true band gap, an example of which is shown for $W_D = 0$ and $W_Q = 0.55t$ in Fig. 3(d). In each case, introducing disorder smoothly fills in these band gaps, pseudogaps, and fine features while rounding out the sharp structure that is due to quasiperiodicity.

To determine the location of the AQCP at finite disorder and quasiperiodic potential strength we evaluate $\rho''(0)$ for fixed W_Q as a function of W_D to determine the location of the peak in $\rho''(0)$, as shown in Figs. 3(b) and 3(e), which provides an accurate estimate of the AQCP crossover location $W_A(W_Q)$. Importantly, these data are converged in system size L and KPM expansion order N_C , and there is no divergence of $\rho''(0)$ upon increasing either L or N_C , demonstrating the crossover nature of the AQCP. Doing this across the parameter regime results in the phase diagram shown in Fig. 1. We note that the phase boundary is obtained for a fixed system size $L = 89$ and KPM expansion order $N_C = 2^{10}$, and very close to the MAT at small W_D it could be weakly shifted. Remarkably, the AQCP smoothly connects from the termination of the small diffusive metal phase due to the first magic-angle transition at $W_Q = W'_{M,1}$ to the second magic-angle transition near $W_Q = W_{MA,2} \approx 0.63t$. Comparing the crossover boundary in Fig. 1 with the estimates of the velocity of the disorder-free model $v(W_Q)$ shown in Fig. 2 demonstrates that the line of avoided transitions $W_A(W_Q)$ is simply parameterized by the relation

$$W_A(W_Q) \propto v(W_Q) \quad (10)$$

for $W_Q < W_{M,1}$. This relation inside the semimetal phase demonstrates that in the low-energy limit the only relevant scale left in the problem is the Weyl cone velocity $v(W_Q)$, which we comment on in more detail at the end of this section.

In Fig. 1 we compare the line of AQCPs between Gaussian and binary disorder distributions. The distinction between these two distributions is significant only at sufficiently weak W_Q . This can be understood as follows: As we increase the quasiperiodic potential strength (with $W_D = 0$), a semimetal miniband forms around zero energy for $W_Q \gtrsim 0.15t$ with a hard gap [e.g., Fig. 3(a)] and a new effective mini Brillouin zone of linear size $(\pi - Q)/a$ (where $a = 1$ denotes the lattice spacing). As a result, an emergent unit cell develops that goes from size a to $a_{MB} = a \frac{2\pi}{(\pi - Q)} \approx 8.5a$. The density of states before and after this first miniband has opened is shown in the Appendix. As the magic-angle transition is approached further, lower-energy minibands continue to appear [46]. If we then project the Hamiltonian onto the lowest-energy miniband, which is separated from the rest of the states by a hard gap via the projection operator $\hat{P}_{MB} = \sum_{E_n \in MB} |E_n\rangle\langle E_n|$ (which sums over energy eigenstates with energies within the miniband), we can then compute Wannier states on the lowest-energy miniband. Thanks to the hard gaps and no topology in the band structure, these are exponentially localized to Wannier centers [58] labeled by \mathbf{R} on the moiré lattice with the Wannier functions $W_{\mathbf{R}}(\mathbf{r})$. Applying this unitary operation plus a projection onto the lowest-energy miniband maps the disorder potential in the Hamiltonian to $\sum_{\mathbf{r}} V_D(\mathbf{r}) \psi_{\mathbf{r}}^\dagger \psi_{\mathbf{r}} \rightarrow \sum_{\mathbf{R}} \tilde{V}_D(\mathbf{R}) \psi_{\mathbf{R}}^\dagger \psi_{\mathbf{R}}$, where \mathbf{R} labels the Wannier centers and

$$\tilde{V}_D(\mathbf{R}) = \sum_{\mathbf{r} \in a_{MB}} V(\mathbf{r}) |W_{\mathbf{R}}(\mathbf{r})|^2 \quad (11)$$

is the coarse-grained random potential on the scale of the moiré unit cell. As a result, the sharp distinction between the Gaussian potential, which has large local fluctuations, and the binary distribution, which does not, is lost after coarse graining over this larger unit cell. This conclusion is consistent with the lack of distinction between Gaussian and binary disorders in the vicinity of each magic-angle transition.

Now turning on finite disorder strength at a fixed value of W_Q (which remains in the semimetal phase), we expect that a nonzero density of states will be induced at the Weyl node energy due to rare-region effects. As shown in Figs. 3(c) and 3(f), we find that the DOS is converged in N_C and goes as

$$\ln \rho(0) \sim -\frac{A(W_Q)}{W_D^2} \quad (12)$$

(for each value W_Q that is in the semimetal phase of the model for $W_D = 0$). From fits to this rare-region form shown in Figs. 3(c) and 3(f), we extract $A(W_Q)$. At weak disorder and quasiperiodicity strength we find good agreement with the identification

$$A(W_Q) \propto v(W_Q)^2, \quad (13)$$

as demonstrated in Fig. 2 by comparing $A(W_Q)$ to the numerically estimated value of $v(W_Q)$ from $\rho''(0)$. However, we do find a distinction at larger quasiperiodic strengths $W_Q \gtrsim 0.5t$, where the Weyl semimetal miniband is no longer isolated from the rest of the states by a hard gap such as in

Fig. 3(d) (this minigap closure occurs near $W \approx 0.5t$, which is not shown), which alters the shape of the cutoff function and energy dramatically. Correspondingly, the prefactor in the DOS $A(W_Q)$ does not simply follow $v(W_Q)$ in this regime ($W_Q \gtrsim 0.5t$).

The data in Fig. 2 and results in Eqs. (10) and (13) suggest that in the semimetal phase there is only one relevant scale $v(W_Q)$, which is described by the following picture. For a Weyl semimetal in the presence of disorder, the low-energy continuum model $H = v\mathbf{k} \cdot \boldsymbol{\sigma} + V(\mathbf{x})$ has one dimensionless parameter that controls the physics: $\alpha_D = W_D/(v/a)$ for disorder strength W_D , velocity v , and cutoff (lattice) scale a . As the length scale is not varied in this problem, only $v = v(W_Q)$ at low energy, suggesting $W_A \sim v(W_Q)$, as we find. In a similar manner, the density of states should be exponentially suppressed by $\ln \rho(0) \sim -1/\alpha_D^2 \sim -v(W_Q)^2/W_D^2$. This simple single parameter which controls the low-energy theory is consistent with all of the data, allowing us to even discover properties of the low-energy Hamiltonian. It further lends credence to the statement that what we are witnessing is physics occurring due to the Weyl point itself and not another structure imposed by, say, the myriad gaps opened by either subtle tight-binding model effects or the fine structure emerging at higher energies due to quasiperiodicity.

IV. APPROACHING THE MAT ALONG THE LINE OF AQCPs

Having identified the crossover boundaries marked by the line of AQCPs, defined by the disorder strength $W_D = W_A(W_Q)$ that terminates at the magic angles, i.e., $W_A(W_{MA}) = 0$, we now study the critical properties of the magic-angle transition. The inclusion of disorder allows us to approach the magic-angle transition from the line of avoided transitions, which effectively parametrize the path through parameter space of maximal correlation length (as a function of W_D) for each value of W_Q . As the critical properties of each magic-angle transition remain the same, without loss of generality, we focus on the second magic angle that occurs for $W_{M,2}/t \approx 0.63$ and approach it from below. This is also convenient because the close proximity of the two transitions $W_{M,1}$ and $W'_{M,1}$ (see Fig. 1) that we expect will make the numerical study below more challenging.

Figures 4(a) and 4(b) show the energy dependence of the density of states along the line of avoided transitions terminating at $W = W_{MA,2}$. At each avoided critical point the density of states develops the scaling at finite energy $[|E| > |E^*|]$, where E^* marks the crossover energy set by the finite value of $\rho(0)$,

$$\rho(|E| > |E^*|) \sim |E|, \quad (14)$$

where this power law is consistent with the one-loop renormalization group results that produce a dynamic exponent $z = 3/2$ [32]. We note that this energy dependence is seen at each avoided transition [i.e., maximum in $\rho''(0)$ versus W_D], as also seen in Figs. 3(a) and 3(d). However, at the AQCP and sufficiently low energy, the density of states is nonzero $\rho(0) > 0$ [as exemplified in Figs. 3(c) and 3(f) and Eq. (12)], which rounds out this power law. At the MAT, on the other hand (with $W_D = 0$), $\rho(0)$ is nonzero, as seen in Fig. 4(b). One

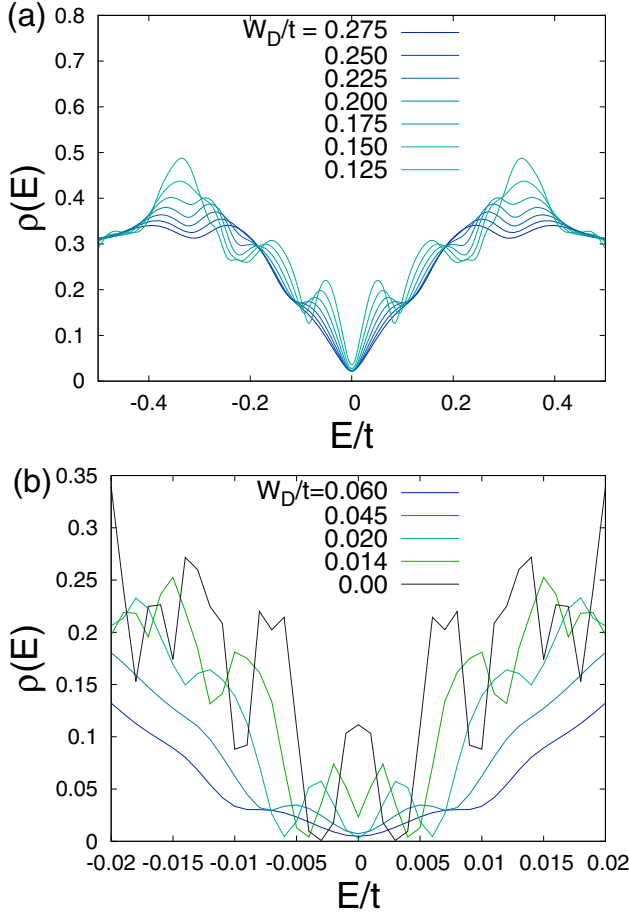


FIG. 4. Density of states along the line of AQCPs that is defined by $W_A(W_Q)$. We show $\rho(E)$ for $L = 89$ at larger $W_D = W_A(W_Q)$ in (a) (with $N_C = 2^{13}$) and closer to the transition at a much lower energy scale in (b) (with $N_C = 2^{14}$) as $W_A \rightarrow 0$ [recall $W_A(W_Q)$ is shown in the phase diagram in Fig. 1]. The data are shown starting from $W_Q = 0.55t$ and terminating at the magic-angle transition at $W_Q^c = 0.6345t$ for $W_D = 0$. The finite but low-energy dependence along the line of AQCPs is consistent with the expected behavior in Eq. (14). However, as we go from (a) to (b), we can see that a consequence of the second miniband opening up for $W_Q \approx 0.62t$ realizes a dramatically renormalized $\rho''(0)$ seen through the shape near zero energy until we hit the MAT and a finite density of states is generated ($W_D = 0$).

can clearly see that the slope of the linear part of the density of states that follows Eq. (14) is monotonically increasing as we approach the MAT, which is directly reflected in the behavior of $\rho(E)$ and $\rho''(0)$ at the lowest energies, which we now come to.

First, we recall that $\rho''(0)$ diverges at the magic-angle transition [44]; approaching this singular behavior from finite disorder strength allows us to approach the magic-angle transition in a unique way to probe the critical scaling properties. We first focus on $\rho''(0)$ along $W_A(W_Q)$ at large enough KPM expansion order to resolve the second miniband opening near $W_Q \approx 0.62t$ ($W_D = 0$) in Fig. 5(a). We show how this second miniband appears in the Appendix. Before the second miniband opens ($W_Q < 0.62t$) we see a single clear maximum in $\rho''(0)$. In contrast after the second mini-

band has opened ($W_Q > 0.62t$), we see the AQCP becomes significantly sharper, leaving behind a second peak. While we are able to converge both of these peaks in N_C for $W_Q = 0.625t$ as shown Fig. 5(b), that is not possible as we get closer to the MAT. As an example, we show $W_Q = 0.63t$ in Fig. 5(c); while we are able to converge the weaker peak at larger W_D , we cannot converge the sharper weak at weaker disorder strength.

In order to associate these two peaks with AQCPs in the first and second minibands we show the evolution of $\rho(E)$ at fixed $W_Q = 0.63t$ as a function of W_D in Fig. 6. Importantly, we find that at each peak in $\rho''(0)$, $\rho(E)$ follows the expected AQCP “scaling” form in Eq. (14). As the value of $\rho''(0)$ is significantly larger and not fully converged in N_C for the second miniband, we now turn to how this begins to diverge as we come to the MAT.

Focusing on $\rho''(0)$ along the avoided line, we plot it versus $W_A(W_Q)$ as we approach the MAT in Fig. 7(a) for both the dominant peak and the subleading peak, while the inset shows the location of each maximum in $\rho''(0)$. As we previously described, we are able to converge the dominant peak in N_C when we are far enough away from the MAT. This regime, which is controlled by the first miniband, is well described by the partial power law

$$\rho''(0) \sim \frac{1}{(W_A)^2} \quad \text{in miniband 1,} \quad (15)$$

and this also describes the well-converged peak (which is also associated with miniband 1). We pause here to note that if this power law were to hold all the way to $W_A = 0$, we would, in fact, find our results to not be internally consistent. To understand why consider the following: We established in Eq. (10) that $W_A \sim v(W_Q)$, but this implies that the density of states diverges as $\rho''(0) \sim 1/v(W_Q)^2$, a slower divergence than in the clean limit $W_D = 0$, where $\rho''(0) \sim 1/v(W_Q)^3$, a contradiction. This issue is alleviated, however, by considering how the second miniband enhances $\rho''(0)$.

The nature in which $\rho''(0)$ is increasing in the second miniband, on the other hand, is stronger, where our limited numerical data yield the partial power law

$$\rho''(0) \sim \frac{1}{(W_A)^{2.5}} \quad \text{in miniband 2.} \quad (16)$$

Importantly, the combination of this increase in the partial power law exponent and the demonstration that its value is miniband dependent resolves the prior internal inconsistency with the limit of $W_D = 0$. To look at this partial divergence within the second miniband in a different way, we consider $\rho''(0)$ as a function of N_C along W_A from where we can to where we cannot converge $\rho''(0)$. Precisely at the MAT $W_D = 0$ and $W_Q = 0.6345t$, we find $\rho''(0)$ diverges with N_C as $\rho''(0) \sim (N_C)^{2.5}$ for the largest N_C that we have accessed.

This leads us to argue that as we approach the MAT, each miniband produces a partial power-law-like divergence of $\rho''(0)$ with $1/(W_A)$ that is described by

$$\rho''(0) \sim \frac{1}{(W_A)^{\beta_n}} \quad \text{in miniband } n \quad (17)$$

where β_n depends on the n th miniband; in the present problem we find $\beta_1 \approx 2$ and $\beta_2 \approx 2.5$. As two of us conjectured in

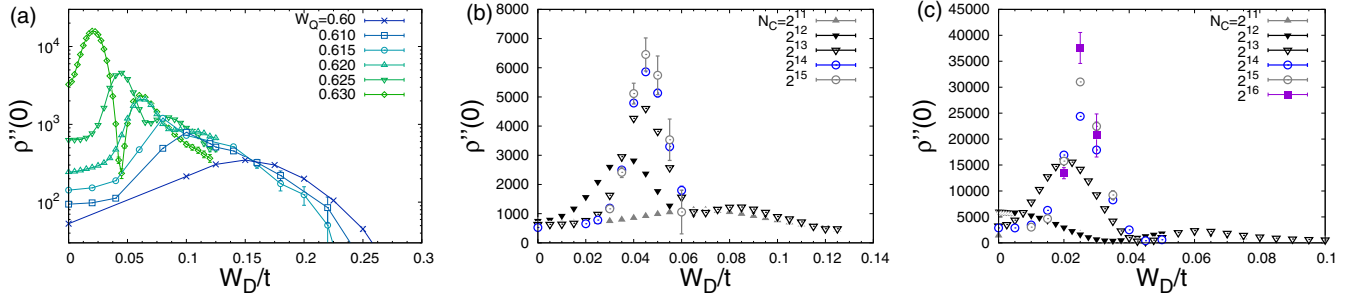


FIG. 5. Evolution of the AQCP on approach to the magic-angle transition along $W_A(W_Q)$. (a) Focusing on $\rho''(0)$ on approach to the transition for $N_C = 2^{13}$, we see that the original peak that we associate with the AQCP splits off, leaving behind a much weaker second peak at larger W_D that can be associated with an approximate AQCP due to the parts of the band outside of the second miniband. (b) We study the evolution of the peaks for $W_Q = 0.625t$ as a function of the expansion order, demonstrating a converged AQCP peak at this system size ($L = 89$). (c) However, for $W_Q = 0.63t$ as we get closer to the MAT, we are unable to converge the peak [see also Fig. 7(b)].

Ref. [46], there should be an infinite sequence of minibands opening up as we get exponentially closer to the MAT so that each corresponds to a given order in perturbation theory that is dictated by the irrational nature of the incommensurate wave vector Q in Eq. (5). Here it is the sequence $F_{3n}/2$, where F_m are Fibonacci numbers; the sequence represents the denominators of the continued fraction of $\sqrt{5}$. As a result, we conjecture that along the line of AQCPs there is an infinite sequence of β_n ; obtaining β_3 in our problem, however, remains a challenging computational task.

V. DISCUSSION

In this paper, we made a direct link between disorder-driven avoided quantum criticality and the semimetal-to-diffusive metal magic-angle phase transitions tuned by

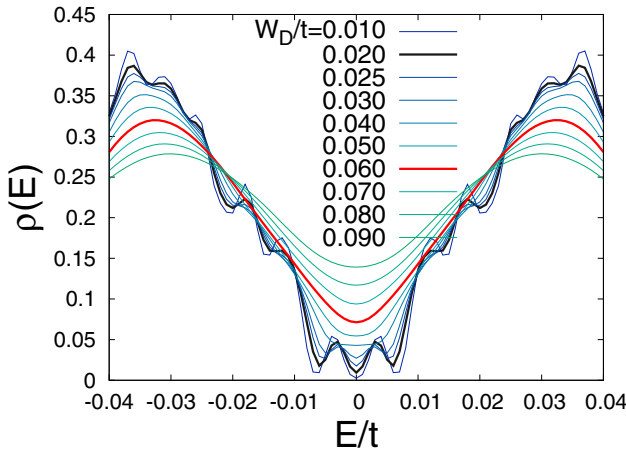


FIG. 6. Demonstration of AQCPs in the first and second minibands for $W_Q/t = 0.63$. We show the density of states $\rho(E)$ as a function of energy E for $L = 89$ and $N_C = 2^{13}$ at the first maximum in $\rho''(0)$ in black, depicting the scaling $\rho(E) \sim |E|$ in the second miniband. The location of the second weaker peak in $\rho''(0)$ is marked in red, depicting the scaling $\rho(E) \sim |E|$ in the first miniband. For reference, see Fig. 5(a) for the structure of $\rho''(0)$. At each peak in $\rho''(0)$ we find the low-energy dependence follows the AQCP form in Eq. (14), allowing us to identify the signatures of two AQCPs as a function of W_D sufficiently close to the MAT.

quasiperiodicity. By viewing the problem as adding disorder to the quasiperiodic model, we constructed a complete phase diagram. The quasiperiodic potential renormalizes the Weyl semimetal parameters, and away from the magic-angle transitions the Weyl semimetal survives. Adding disorder to this system fills in the band gaps and pseudogaps due to quasiperiodicity, introduces a finite density of states at the Weyl node due to rare regions of the random potential, and rounds out the magic-angle transition into a crossover. The line of crossovers is parameterized by the Weyl cone velocity renormalized by the quasiperiodic potential. Last, the divergence of $\rho''(0)$ (or the vanishing of the Weyl velocity) at the magic-angle transition was computed by approaching the transition along the lines of avoided critical points. In future work, it will be interesting to also study the effects of disorder along the two MATs at smaller W_Q in Fig. 1 than we considered here.

The disordered and quasiperiodic Weyl semimetal model we expect can be realized in future realizations of ultra-cold atom experiments that use 3D spin-orbit coupling to realize a Weyl semimetal phase. Disorder can be introduced using several approaches (e.g., speckle patterns [59], programmable potentials [60,61], digital mirror devices [62]), while quasiperiodicity can be achieved through a second optical lattice incommensurate with the first. The phase transition and crossovers can be measured through time of flight imaging of wave packet dynamics [63] as well as through the spectral function measured using radio-frequency spectroscopy [57,64]. It will be exciting to see whether the transition and its connection to avoided quantum criticality can be exposed in future experiments. Alternatively, circuit quantum electrodynamic setups were proposed by one of us to also realize this phenomenon and see its effect on spectroscopic transport measurements of the junctions [65,66].

Future theoretical work needs to utilize a graphical processing unit (GPU) implementation of the KPM to make further progress. To see further minibands open up as we get exponentially close to the magic-angle transition we would have to systematically increase the system size beyond the value of $L = 89$ that we considered here, which revealed the second miniband at these expansion orders. In fact, the sequence of perturbation theory order needed to see the next

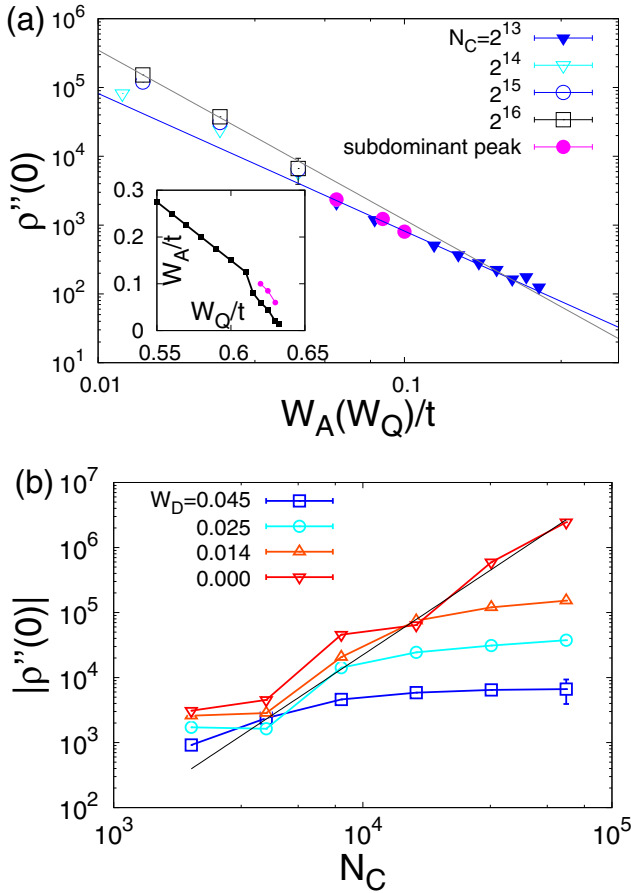


FIG. 7. Divergence of $\rho''(0)$ on the approach to the MAT along the line of AQCPs. (a) The solid data points represent peaks in $\rho''(0)$ that are converged in N_C that follow $\rho''(0) \sim 1/W_A^2$ (the blue solid line is a fit). The open symbols are not yet converged [although they are close to being converged as depicted in (b)], and we show their N_C dependence, with a fit to the largest $N_C = 2^{16}$ (gray line), yielding $\rho''(0) \sim 1/W_A^{2.5}$. Inset: The locations of the leading AQCPs $W_A(W_Q)$ are shown as black symbols, while the location of the subdominant peak is shown as magenta circles. (b) Dependence of the peak in $\rho''(0)$ on the KPM expansion order N_C as we approach the MAT along the line of AQCPs. At the MAT ($W_D = 0$) we find this diverges as $\rho''(0) \sim (N_C)^{2.5}$ (the fit to the largest three expansion orders is shown as a black line). All data here are obtained for a system size $L = 89$.

gap open [46] up gives us a clue for this: If we take $L = 3, 5$, the first miniband opens up, but the unit cell size is the entire size of the system (and hence cannot be disordered); for $L = 13, 21$, the second miniband forms, and the first miniband can begin to become disordered. For $L = 55, 89$ the second miniband can be disordered, while the third miniband forms as only one unit cell. (Note that we skip even numbers since this degenerate case puts the new miniband gap precisely at zero energy, and no new miniband has yet been formed.) Following this pattern, in order to begin to see disorder effects in the third miniband, we would need to access $L = 233, 377$ (which are accessible with GPU implementations of the KPM). While continuing this process indefinitely will quickly lead to prohibitively large system sizes, this issue may also be improved by a renormalization scheme when $W_D/t \ll 1$ that focuses

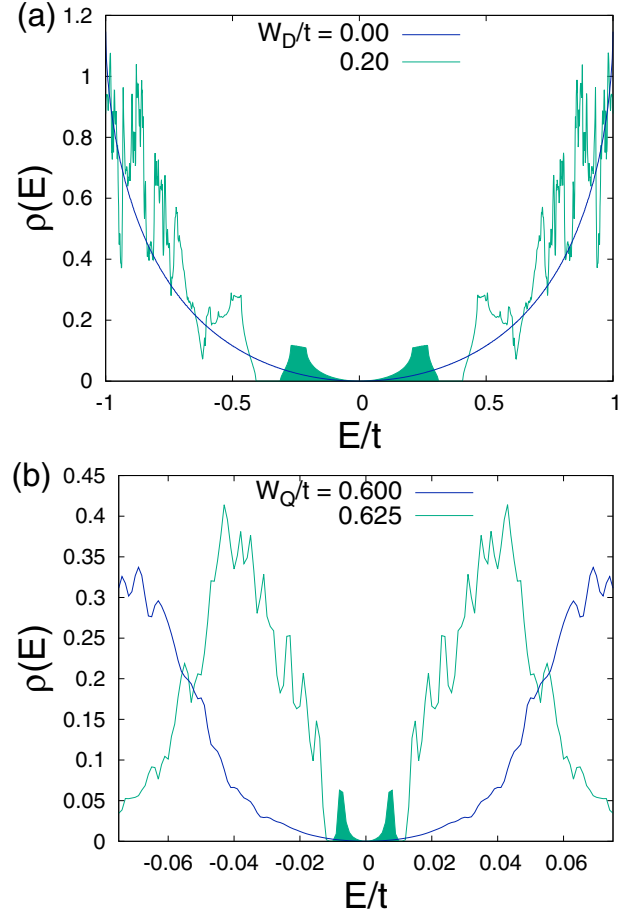


FIG. 8. Minibands in the clean limit, $W_D = 0$: For clarity, we show the density of states in the clean limit for values of W_Q that are less than and greater than required to open (a) the first miniband and (b) the second miniband, both of which are shaded green, but the energy scale is much smaller in the second miniband. Both minibands depict the expected Weyl scaling $\rho(E) \sim E^2$ at sufficiently low energy with very different coefficients. The results in (a) are for $L = 89, 1000$ samples, and $N_C = 2^{13}$, while (b) is for $L = 89$ and 5000 samples, where $W_Q = 0.6t$ has $N_C = 2^{13}$ but for $W_Q = 0.625t$ we take $N_C = 2^{14}$ in order to show hard gaps as the second miniband forms. We also point the reader to Ref. [44] for more data on the opening of the first miniband.

computational effort on the lowest available miniband, which we leave for future work.

ACKNOWLEDGMENTS

We thank S. Das Sarma, S. Gopalakrishnan, and E. König for useful discussions. J.H.P. is partially supported by NSF CAREER Grant No. DMR-1941569 and the Alfred P. Sloan Foundation through a Sloan Research Fellowship. Part of this work was performed at the Aspen Center for Physics, which is supported by National Science Foundation Grant No. PHY-2210452 (J.H.W., J.H.P.), as well as the Kavli Institute of Theoretical Physics, which is supported in part by the National Science Foundation under Grants No. NSF PHY-1748958 and No. PHY-2309135 (J.H.W., J.H.P.). D.A.H. was supported in part by NSF QLCI Grant No. OMA-2120757.

The authors acknowledge the following research computing resources: the Beowulf cluster at the Department of Physics and Astronomy of Rutgers University and the Amarel cluster from the Office of Advanced Research Computing (OARC) at Rutgers, The State University of New Jersey.

APPENDIX: MINIBANDS IN THE DISORDER FREE LIMIT

In this Appendix, we briefly review the formation of the first and second minibands observed in the main text without disorder. The quasiperiodic potential connects two of the neighboring Weyl cones of opposite helicity at finite energy [e.g., scattering between the Weyl cone at $\mathbf{K} = (0, 0, 0)$

and $\mathbf{K} = (\pi, 0, 0)$]; the leading scattering process then connects momentum k with $\pi - k$ such that $k + Q_L = \pi - k$, and once the potential is strong enough, this will open a gap at this energy (which can be described with degenerate perturbation theory). For this leading perturbative effect this carves out a mini Brillouin zone of size $(\pi - Q_L)^3$. If we focus on $Q_L = 2\pi F_{n-2}/L$, the first miniband has $N_1 = 2(F_{n-3})^3$ states [44,47]. The second miniband arises due to fourth-order perturbation theory with a momentum transfer $4Q_L - 3\pi$ and has $N_2 = 2(F_{n-6})^3$ states. For the data shown in Fig. 8 (at $L = 89$) this yields 18 522 states in miniband 1 in Fig. 8(a) and 250 states in miniband 2 in Fig. 8(b), which is excellent agreement with our numerical data.

-
- [1] S. Borisenko, Q. Gibson, D. Evtushinsky, V. Zabolotnyy, B. Büchner, and R. J. Cava, Experimental realization of a three-dimensional Dirac semimetal, *Phys. Rev. Lett.* **113**, 027603 (2014).
 - [2] Z. Liu *et al.*, Discovery of a three-dimensional topological Dirac semimetal, Na_3Bi , *Science* **343**, 864 (2014).
 - [3] M. Neupane *et al.*, Observation of a three-dimensional topological Dirac semimetal phase in high-mobility Cd_3As_2 , *Nat. Commun.* **5**, 3786 (2014).
 - [4] B. Q. Lv, H. M. Weng, B. B. Fu, X. P. Wang, H. Miao, J. Ma, P. Richard, X. C. Huang, L. X. Zhao, G. F. Chen, Z. Fang, X. Dai, T. Qian, and H. Ding, Experimental discovery of Weyl semimetal TaAs, *Phys. Rev. X* **5**, 031013 (2015).
 - [5] B. Q. Lv, N. Xu, H. M. Weng, J. Z. Ma, P. Richard, X. C. Huang, L. X. Zhao, G. F. Chen, C. E. Matt, F. Bisti, V. N. Strocov, J. Mesot, Z. Fang, X. Dai, T. Qian, M. Shi, and H. Ding, Observation of Weyl nodes in TaAs, *Nat. Phys.* **11**, 724 (2015).
 - [6] S.-Y. Xu *et al.*, Discovery of a Weyl fermion semimetal and topological Fermi arcs, *Science* **349**, 613 (2015).
 - [7] S.-Y. Xu *et al.*, Discovery of a Weyl fermion state with Fermi arcs in niobium arsenide, *Nat. Phys.* **11**, 748 (2015).
 - [8] S.-Y. Xu *et al.*, Experimental discovery of a topological Weyl semimetal state in TaP, *Sci. Adv.* **1**, e1501092 (2015).
 - [9] N. Xu, H. M. Weng, B. Q. Lv, C. E. Matt, J. Park, F. Bisti, V. N. Strocov, D. Gawryluk, E. Pomjakushina, K. Conder, N. C. Plumb, M. Radovic, G. Autès, O. V. Yazyev, Z. Fang, X. Dai, T. Qian, J. Mesot, H. Ding, and M. Shi, Observation of Weyl nodes and Fermi arcs in tantalum phosphide, *Nat. Commun.* **7**, 11006 (2016).
 - [10] F. F. Tafti, J. J. Ishikawa, A. McCollam, S. Nakatsuji, and S. R. Julian, Pressure-tuned insulator to metal transition in $\text{Eu}_2\text{Ir}_2\text{O}_7$, *Phys. Rev. B* **85**, 205104 (2012).
 - [11] A. B. Sushkov, J. B. Hofmann, G. S. Jenkins, J. Ishikawa, S. Nakatsuji, S. Das Sarma, and H. D. Drew, Optical evidence for a Weyl semimetal state in pyrochlore $\text{Eu}_2\text{Ir}_2\text{O}_7$, *Phys. Rev. B* **92**, 241108(R) (2015).
 - [12] H.-H. Lai, S. E. Grefe, S. Paschen, and Q. Si, Weyl-Kondo semimetal in heavy-fermion systems, *Proc. Natl. Acad. Sci. USA* **115**, 93 (2018).
 - [13] P.-Y. Chang and P. Coleman, Parity-violating hybridization in heavy Weyl semimetals, *Phys. Rev. B* **97**, 155134 (2018).
 - [14] P. Telang, K. Mishra, G. Prando, A. K. Sood, and S. Singh, Anomalous lattice contraction and emergent electronic phases in $\text{Eu}_2\text{Ir}_2\text{O}_7$, *Phys. Rev. B* **99**, 201112(R) (2019).
 - [15] S. Dzsaber, X. Yan, M. Taupin, G. Eguchi, A. Prokofiev, T. Shiroka, P. Blaha, O. Rubel, S. E. Grefe, H.-H. Lai, Q. Si, and S. Paschen, Giant spontaneous Hall effect in a nonmagnetic Weyl-Kondo semimetal, *Proc. Natl. Acad. Sci. USA* **118**, e2013386118 (2021).
 - [16] K. Kuroda *et al.*, Evidence for magnetic Weyl fermions in a correlated metal, *Nat. Mater.* **16**, 1090 (2017).
 - [17] C. Y. Guo, F. Wu, Z. Z. Wu, M. Smidman, C. Cao, A. Bostwick, C. Jozwiak, E. Rotenberg, Y. Liu, F. Steglich, and H. Q. Yuan, Evidence for Weyl fermions in a canonical heavy-fermion semimetal YbPtBi , *Nat. Commun.* **9**, 4622 (2018).
 - [18] X. Liu, S. Fang, Y. Fu, W. Ge, M. Kareev, J.-W. Kim, Y. Choi, E. Karapetrova, Q. Zhang, L. Gu, E.-S. Choi, F. Wen, J. H. Wilson, G. Fabbri, P. J. Ryan, J. W. Freeland, D. Haskel, W. Wu, J. H. Pixley, and J. Chakhalian, Magnetic Weyl semimetallic phase in thin films of $\text{Eu}_2\text{Ir}_2\text{O}_7$, *Phys. Rev. Lett.* **127**, 277204 (2021).
 - [19] Z. Liu *et al.*, A stable three-dimensional topological Dirac semimetal Cd_3As_2 , *Nat. Mater.* **13**, 677 (2014).
 - [20] S.-Y. Xu *et al.*, Observation of Fermi arc surface states in a topological metal, *Science* **347**, 294 (2015).
 - [21] S.-M. Huang *et al.*, A Weyl Fermion semimetal with surface Fermi arcs in the transition metal monophosphide TaAs class, *Nat. Commun.* **6**, 7373 (2015).
 - [22] H. Weng, C. Fang, Z. Fang, B. A. Bernevig, and X. Dai, Weyl semimetal phase in noncentrosymmetric transition-metal monophosphides, *Phys. Rev. X* **5**, 011029 (2015).
 - [23] H.-J. Kim, K.-S. Kim, J.-F. Wang, M. Sasaki, N. Satoh, A. Ohnishi, M. Kitaura, M. Yang, and L. Li, Dirac versus Weyl fermions in topological insulators: Adler-Bell-Jackiw anomaly in transport phenomena, *Phys. Rev. Lett.* **111**, 246603 (2013).
 - [24] T. Liang, Q. Gibson, M. N. Ali, M. Liu, R. J. Cava, and N. P. Ong, Ultrahigh mobility and giant magnetoresistance in the Dirac semimetal Cd_3As_2 , *Nat. Mater.* **14**, 280 (2015).
 - [25] Q. Li, D. E. Kharzeev, C. Zhang, Y. Huang, I. Pletikosić, A. V. Fedorov, R. D. Zhong, J. A. Schneeloch, G. D. Gu, and T. Valla, Chiral magnetic effect in ZrTe_5 , *Nat. Phys.* **12**, 550 (2016).

- [26] Z.-Y. Wang, X.-C. Cheng, B.-Z. Wang, J.-Y. Zhang, Y.-H. Lu, C.-R. Yi, S. Niu, Y. Deng, X.-J. Liu, S. Chen, and J.-W. Pan, Realization of an ideal Weyl semimetal band in a quantum gas with 3D spin-orbit coupling, *Science* **372**, 271 (2021).
- [27] S. V. Syzranov and L. Radzihovsky, High-dimensional disorder-driven phenomena in Weyl semimetals, semiconductors, and related systems, *Annu. Rev. Condens. Matter Phys.* **9**, 35 (2018).
- [28] J. Pixley and J. H. Wilson, Rare regions and avoided quantum criticality in disordered Weyl semimetals and superconductors, *Ann. Phys. (NY)* **435**, 168455 (2021).
- [29] R. Shindou and S. Murakami, Effects of disorder in three-dimensional Z_2 quantum spin Hall systems, *Phys. Rev. B* **79**, 045321 (2009).
- [30] Y. Ominato and M. Koshino, Quantum transport in a three-dimensional Weyl electron system, *Phys. Rev. B* **89**, 054202 (2014).
- [31] S. Ryu and K. Nomura, Disorder-induced quantum phase transitions in three-dimensional topological insulators and superconductors, *Phys. Rev. B* **85**, 155138 (2012).
- [32] P. Goswami and S. Chakravarty, Quantum criticality between topological and band insulators in 3+1 dimensions, *Phys. Rev. Lett.* **107**, 196803 (2011).
- [33] S. V. Syzranov, L. Radzihovsky, and V. Gurarie, Critical transport in weakly disordered semiconductors and semimetals, *Phys. Rev. Lett.* **114**, 166601 (2015).
- [34] R. Nandkishore, D. A. Huse, and S. L. Sondhi, Rare region effects dominate weakly disordered three-dimensional Dirac points, *Phys. Rev. B* **89**, 245110 (2014).
- [35] J. H. Pixley, D. A. Huse, and S. Das Sarma, Rare-region-induced avoided quantum criticality in disordered three-dimensional Dirac and Weyl semimetals, *Phys. Rev. X* **6**, 021042 (2016).
- [36] J. H. Pixley, D. A. Huse, and S. Das Sarma, Uncovering the hidden quantum critical point in disordered massless Dirac and Weyl semimetals, *Phys. Rev. B* **94**, 121107 (2016).
- [37] J. H. Pixley, Y.-Z. Chou, P. Goswami, D. A. Huse, R. Nandkishore, L. Radzihovsky, and S. Das Sarma, Single-particle excitations in disordered Weyl fluids, *Phys. Rev. B* **95**, 235101 (2017).
- [38] V. Gurarie, Theory of avoided criticality in quantum motion in a random potential in high dimensions, *Phys. Rev. B* **96**, 014205 (2017).
- [39] M. Buchhold, S. Diehl, and A. Altland, Vanishing density of states in weakly disordered Weyl semimetals, *Phys. Rev. Lett.* **121**, 215301 (2018).
- [40] M. Buchhold, S. Diehl, and A. Altland, Nodal points of Weyl semimetals survive the presence of moderate disorder, *Phys. Rev. B* **98**, 205134 (2018).
- [41] A. Galindo and P. Pascual, *Quantum Mechanics I* (Springer, Berlin, Heidelberg, 2012).
- [42] J. P. S. Pires, B. Amorim, A. Ferreira, Í. Adagideli, E. R. Mucciolo, and J. M. V. P. Lopes, Breakdown of universality in three-dimensional Dirac semimetals with random impurities, *Phys. Rev. Res.* **3**, 013183 (2021).
- [43] J. H. Wilson, D. A. Huse, S. Das Sarma, and J. H. Pixley, Avoided quantum criticality in exact numerical simulations of a single disordered Weyl cone, *Phys. Rev. B* **102**, 100201(R) (2020).
- [44] J. H. Pixley, J. H. Wilson, D. A. Huse, and S. Gopalakrishnan, Weyl semimetal to metal phase transitions driven by quasiperiodic potentials, *Phys. Rev. Lett.* **120**, 207604 (2018).
- [45] V. Mastropietro, Stability of Weyl semimetals with quasiperiodic disorder, *Phys. Rev. B* **102**, 045101 (2020).
- [46] Y. Fu, E. J. König, J. H. Wilson, Y.-Z. Chou, and J. H. Pixley, Magic-angle semimetals, *npj Quantum Mater.* **5**, 1 (2020).
- [47] Y.-Z. Chou, Y. Fu, J. H. Wilson, E. J. König, and J. H. Pixley, Magic-angle semimetals with chiral symmetry, *Phys. Rev. B* **101**, 235121 (2020).
- [48] Y. Fu, J. H. Wilson, and J. H. Pixley, Flat topological bands and eigenstate criticality in a quasiperiodic insulator, *Phys. Rev. B* **104**, L041106 (2021).
- [49] R. Bistritzer and A. H. MacDonald, Moiré bands in twisted double-layer graphene, *Proc. Natl. Acad. Sci. USA* **108**, 12233 (2011).
- [50] M. Gonçalves, H. Z. Olyaei, B. Amorim, R. Mondaini, P. Ribeiro, and E. V. Castro, Incommensurability-induced sub-ballistic narrow-band-states in twisted bilayer graphene, *2D Mater.* **9**, 011001 (2022).
- [51] C. Janot, *Quasicrystals: A Primer* (Clarendon Press, Oxford, UK, 1995).
- [52] T. E. Beechem, T. Ohta, B. Diaconescu, and J. T. Robinson, Rotational disorder in twisted bilayer graphene, *ACS Nano* **8**, 1655 (2014).
- [53] J. H. Wilson, Y. Fu, S. Das Sarma, and J. H. Pixley, Disorder in twisted bilayer graphene, *Phys. Rev. Res.* **2**, 023325 (2020).
- [54] A. Uri *et al.*, Mapping the twist-angle disorder and Landau levels in magic-angle graphene, *Nature (London)* **581**, 47 (2020).
- [55] B. Padhi, A. Tiwari, T. Neupert, and S. Ryu, Transport across twist angle domains in moiré graphene, *Phys. Rev. Res.* **2**, 033458 (2020).
- [56] S. Joy, S. Khalid, and B. Skinner, Transparent mirror effect in twist-angle-disordered bilayer graphene, *Phys. Rev. Res.* **2**, 043416 (2020).
- [57] J. Yi, E. J. König, and J. H. Pixley, Low energy excitation spectrum of magic-angle semimetals, *Phys. Rev. B* **106**, 195123 (2022).
- [58] N. Marzari, A. A. Mostofi, J. R. Yates, I. Souza, and D. Vanderbilt, Maximally localized Wannier functions: Theory and applications, *Rev. Mod. Phys.* **84**, 1419 (2012).
- [59] J. W. Goodman, *Speckle Phenomena in Optics: Theory and Applications* (Roberts, Greenwood Village, CO, 2007).
- [60] C. Monroe, W. C. Campbell, L.-M. Duan, Z.-X. Gong, A. V. Gorshkov, P. W. Hess, R. Islam, K. Kim, N. M. Linke, G. Pagano, P. Richerme, C. Senko, and N. Y. Yao, Programmable quantum simulations of spin systems with trapped ions, *Rev. Mod. Phys.* **93**, 025001 (2021).
- [61] F. A. An, K. Padavić, E. J. Meier, S. Hegde, S. Ganeshan, J. H. Pixley, S. Vishveshwara, and B. Gadway, Interactions and mobility edges: Observing the generalized Aubry-André model, *Phys. Rev. Lett.* **126**, 040603 (2021).
- [62] D. Stuart and A. Kuhn, Single-atom trapping and transport in DMD-controlled optical tweezers, *New J. Phys.* **20**, 023013 (2018).
- [63] P. D. Lett, R. N. Watts, C. I. Westbrook, W. D. Phillips, P. L. Gould, and H. J. Metcalf, Observation of atoms laser

- cooled below the Doppler limit, [Phys. Rev. Lett. **61**, 169 \(1988\)](#).
- [64] S. Gupta, Z. Hadzibabic, M. W. Zwierlein, C. A. Stan, K. Dieckmann, C. H. Schunck, E. G. M. van Kempen, B. J. Verhaar, and W. Ketterle, Radio-frequency spectroscopy of ultracold fermions, [Science **300**, 1723 \(2003\)](#).
- [65] T. Herrig, J. H. Pixley, E. J. König, and R.-P. Riwar, Quasiperiodic circuit quantum electrodynamics, [npj Quantum Inf. **9**, 116 \(2023\)](#).
- [66] T. Herrig, C. Koliofoti, J. H. Pixley, E. J. König, and R.-P. Riwar, Emulating moiré materials with quasiperiodic circuit quantum electrodynamics, [arXiv:2310.15103](#).